Simulation Study of Clinical PET Scanners With Different Geometries, Including TOF and DOI Capabilities

Gabriel Cañizares, Santiago Jiménez-Serrano, Alejandro Lucero, Constantino Morera-Ballester, Enrique Muñoz, José M. Benlloch, and Antonio J. González, *Member, IEEE*

***Abstract*—Total body positron emission tomography (TB-PET) scanners provide high-quality images due to the large sensitivity. Our motivation is to design a TB-PET system with up to 70 cm axial coverage that mitigates the parallax error degradation by using a detector concept based on semi-monolithic LYSO crystals. Furthermore, this detector approach allows to simultaneously reach an accurate coincidence time resolution (CTR) to enhance the image quality by means of time-of-flight (TOF) reconstruction algorithms. We have simulated and compared two positron emission tomography (PET) prototypes with about 70 cm but a different number of detector rings (7 versus 5). The NEMA NU 2 2018 protocol has been implemented. By correcting the parallax error with the depth-of-interaction (DOI) information, the spatial resolution remains homogeneous and below 3 mm in the entire field of view (FOV), differently from designs based on pixelated crystals. The sensitivity reaches values of 58 and 115 cps/kBq, for the 5 and 7 rings configurations, respectively. The noise equivalent count rate (NECR) was found at 563 kcps/mL. This value is lower than other systems, most likely due to the requirement to process a larger number of channels to characterize the DOI. Percent contrasts obtained for two different phantoms are in general beyond 80% for the largest spheres, nearly 100% for the 7 rings configuration once TOF is applied during the reconstruction process. In conclusion, although the sensitivity and NECR results for the 5-rings configuration are lower compared to the 7-rings approach, its overall performance is enhanced by the addition of TOF and parallax error correction, improving that of conventional Whole Body PET scanners (axial length: 20–30 cm) in terms of image quality.**

***Index Terms*—Coincidence time resolution (CTR), depth of interaction (DOI), GATE, positron emission tomography (PET), semi-monolithic detector, simulation.**

Manuscript received 1 December 2023; revised 9 January 2024; accepted 9 February 2024. Date of publication 14 February 2024; date of current version 3 July 2024. This work was supported in part by the Imagen Molecular de Alta Sensibilidad Project Launched by the Conselleria de Sanitat Universal i Salut Publica of the Goverment of Valencia Region, announced in the BOE 328, 28 December 2020, cofounded at 50% by the ERDF, and in part by the European Research Council through the European Union's Horizon 2020 Research and Innovation Program under Agreement 695536. *(Gabriel Cañizares and Santiago Jiménez-Serrano are co-first authors.) (Corresponding author: Santiago Jiménez-Serrano.)*

This work did not involve human subjects or animals in its research.

Gabriel Cañizares is with Full Body Insight, 46520 Sagunto, Spain, and also with the Instituto de Instrumentación para Imagen Molecular, Centro Mixto CSIC—Universitat Politècnica de València, 46022 Valencia, Spain.

Santiago Jiménez-Serrano, Alejandro Lucero, José M. Benlloch, and Antonio J. González are with the Instituto de Instrumentación para Imagen Molecular, Centro Mixto CSIC—Universitat Politècnica de València, 46022 Valencia, Spain (e-mail: sanjiser@i3m.upv.es).

Constantino Morera-Ballester and Enrique Muñoz are with Oncovision, 46022 Valencia, Spain.

Color versions of one or more figures in this article are available at https://doi.org/10.1109/TRPMS.2024.3365911.

Digital Object Identifier 10.1109/TRPMS.2024.3365911

I. Introduction

THE POSITRON emission tomography (PET) technique has been very important in multiple medical protocols such as in therapy assessment or tumor diagnosis [1]. The high clinical specificity and sensitivity of PET, compared to other molecular imaging techniques such as single-photon emission tomography (SPECT), makes it the preferred molecular imaging technique [2]. Moreover, the investigation of new radiotracers leads to an essential improvement in detection specificity [3]. PET scanners do not need collimators, unlike SPECT systems, so their sensitivity is significantly higher. The photons generated in the positron–electron annihilation are highly energetic and therefore PET systems typically use high-density specific inorganic crystals such as BGO or LYSO [4]. Moreover, including time-of-flight (TOF) capabilities in PET [5] improves the image quality of the biomarker distribution inside the patient.

Presently, there is an interest in improving PET scanners capabilities to produce more reliable information. Conventional whole-body PET (WB-PET) scanners have physical sensitivities in the range of 1% [6]. Increasing these sensitivity values would allow one to decrease the injected dose to the patient or reduce the acquisition time, or a combination of both. Some of the solutions to reach this goal are thicker scintillation crystals, organ-dedicated devices, or longer axial PET systems.

Working with thicker scintillation crystals makes it possible to stop more annihilation photons and consequently register them in the system. The main drawback of this approach is observed in a worsening of the energy and time resolutions performance, compared to thinner crystals due to the absorption optical photons [7].

Organ-dedicated PET systems are designed with detectors placed closer to the patient body, so a boost of geometrical sensitivity occurs. Spatial resolution is also improved in comparison with current scanners since higher performance detectors are typically employed [8]. These systems are

ideal for testing novel geometries with a reduced number of detector modules. Other configurations beyond the current ring geometry have been proposed, including a two PET panels design [9], [10] or a decagon geometry [11], [12].

Finally, the third approach has generated general interest in the PET community. While the axial coverage of current WB-PET scanners typically ranges from 20–30 cm, the so-called total-body PET (TB-PET) systems significantly extend beyond this distance by accounting for more detector blocks and rings [13], [14]. This configuration, besides the significant increase in costs, boosts the total sensitivity of the system. Furthermore, it provides information about multiple organs simultaneously, which is very important in the development of new pharmaceutical drugs and other studies [15]. Nowadays, just a few of these scanners exist. For instance, United Imaging Healthcare has developed a scanner called uExplorer with an axial field of view (FOV) of 194 cm and a transaxial FOV of 70 cm [16]. Other examples of TB-PET are the PennPET system developed at the University of Pennsylvania, with an axial coverage that has sequentially increased in the last years, currently reaching 142 cm [17], [18], and a transaxial FOV of 76 cm. The Vision Quadra PET scanner commercialized by Siemens [19], is another example with an axial coverage is 106 cm and a transaxial FOV is 82 cm. A more detailed description of some of these systems will be provided later in this work.

The framework of the present study is based on the project called IMAS, which aims to design, build, and test a TB-PET scanner with an axial coverage of 70 cm. Here, the decision to use a 70-cm axial length was based on balancing the need for sufficient axial length to improve scanner sensitivity and facilitate multiorgan imaging, at a moderated manufacturing cost. This scanner combines, for the first time, the capabilities of correcting the parallax error with depth-of-interaction (DOI) information [20] and precise coincidence time resolution (CTR) [21], [22]. We are implementing a detector configuration in this scanner based on crystal slabs, also called semi-monolithic crystals (see Fig. 1) [23]. In this configuration, the light distribution is characterized in the monolithic axis, allowing the estimation of the DOI. Accurate CTR is also achieved since the scintillation light is constrained to a lower number of photosensors when compared to monolithic crystals, as demonstrated in [24].

In this work, we aim to test, using simulations, two different configurations of a TB-PET scanner with a similar axial coverage of about 70 cm. Both configurations make use of detector rings with roughly 10-cm axial length. In one of the configurations, seven detector rings are used without gaps between detectors in the axial direction, whereas in the second geometry, five rings are used with some gaps between them. This configuration aims to reduce the overall cost without a significant impact in the system performance. Previously, we have analyzed the performance of a 20-cm PET system also based on the same ring configuration [25]. Comparison with the 20-cm axial coverage system and other commercial PET scanners will also be provided.

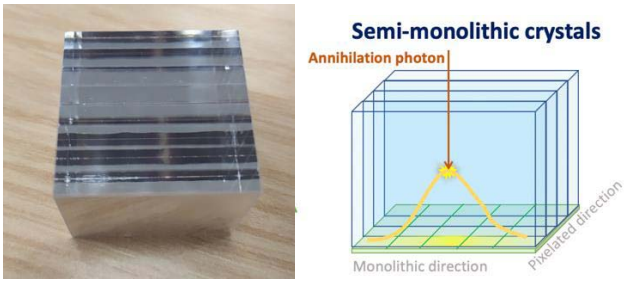

Fig. 1. Left: Photograph of a semi-monolithic crystal array. Right: Sketch of the light distribution inside the slab.

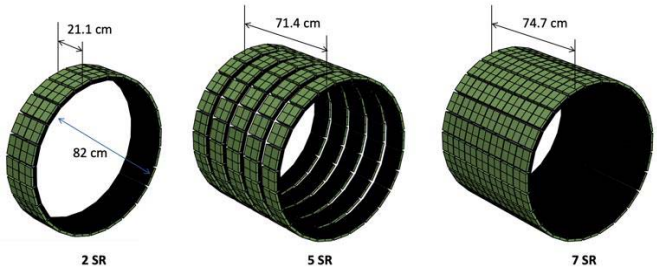

Fig. 2. Sketches and main dimensions for the 2, 5, and 7 SR configurations.

II. Materials and Methods

A. PET Geometries

The detector geometry of the PET configurations is based on LYSO slabs. Each slab size is about $25 \times 3 \times 20$ mm^3 with all faces covered with specular reflectors. Eight of these crystals are merged, with a 3.2-mm pitch, and coupled to an 8×8 SiPM array of 3×3 mm^2 size and 3.2-mm pitch, matching the array of slabs. 4×4 of these blocks, with a gap of 0.3 mm, define the so-called super-module. A ring [dubbed super-ring (SR)] is formed by 24 super-modules, defining a bore diameter of 82 cm and roughly 10 cm in the axial direction. We have implemented in the simulation the 2, 5, and 7 SRs geometry (see Fig. 2). Both the 7 SR and 2 SR geometries have tiny gaps between rings of about 4 mm, corresponding to one virtual pixel in this direction. In the 5 SR configuration, the gap between rings is of about 49 mm, resulting in an axial coverage of 71.4 cm.

B. Gate Simulations

We performed simulations using the Gate v9.0 platform [26] (see Fig. 3), enabling all key functions such as gamma absorption due to the attenuation process, scatter dispersion, and deadtime. A single event is characterized by the optical photon track within the sensitive LYSO volume. It considers the number of Compton interactions that occur and generates a single coordinate calculated using a conventional center of gravity. The energy of the single event was calculated with the sum of all the interactions that deposit energy in the volume, i.e., Compton and Photoelectric. A paralyzable deadtime of 1000 ns was introduced in the singles generation. Lately, a coincidence event was defined every time two single events occur in the same time window, which is set to 3 ns.

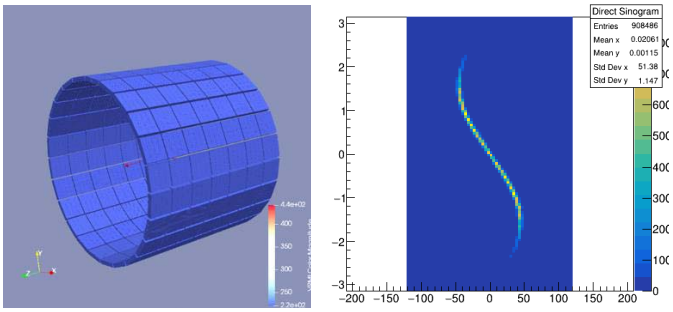

Fig. 3. Left: Simulation representation of the 7 SR configuration. Right: Sinogram of the acquisition of a capillary.

Coincidences of more than 2 events are discarded in the output file. To properly model the different configurations, we have considered certain blurring based on our previously measured hardware detector performance detailed in [27] and [28] and also simulated in [29]. In particular, we introduced the following parameters to the processing chain: an energy resolution of 15% was set at the detector level, combined with a CTR of 330 ps, a spatial resolution of 3 mm in the monolithic axis of the detectors and 5 mm in the DOI direction. Finally, all the registered coincidences are gathered in two possible outputs. The first is a List-Mode file listing the coordinates, energies, and timestamps in binary format for the image reconstruction process. The second output is a sinogram where each angle and distances of the line of response (LOR) are stored in a histogram [30].

C. Image Reconstruction

The List-Mode file accounts for events within a 30% energy window [358–664 keV] around the photopeak. However, during the reconstruction process we considered coincidences of pairs of events whose energy is within a narrower 20% energy window [408–613 keV] around the photopeak. We also considered as scatter coincidences those pairs of events in which one of them has an energy within the range 358–408 keV. Moreover, we only allowed coincidences of one super-module against the opposite 13 super-modules of any ring, defining a useful transaxial FOV of 70 cm.

We performed a DOI correction during the List-Mode file generation for each coincidence event. We calculated the LOR between the two positions at each detector and reassigned the event LOR to the virtual detector pixels intersecting at the entrance surface [31]. Thus, the parallax error can be mitigated.

To obtain the normalization data, we simulated a uniform cylindrical phantom with 70 cm in diameter and 70-cm axial length, which covered the entire FOV of the prototype. This data was also obtained for the 2 SR geometry. 12.8×10^9 coincidences were simulated during the normalization process. Thereafter, the number of counts of all the valid LORs were stored into a sorted histogram. Then, we computed the normalization factors as the ratio of the measured data to the analytical forward projection of the uniform cylinder phantom, normalized by its average. For the calculation of the sensitivity matrix, we performed an analytical backward projection considering one count in each possible LOR for each virtual detector pixel. Furthermore, in order to mitigate the attenuation of events, we generated a synthetic μ-map with the same dimensions as all simulated phantoms.

The normalization factors, the sensitivity matrix, and the corresponding μ-map were fed in a custom-made image reconstruction platform based on the maximum-likelihood expectation–maximization (MLEM) algorithm [32], accelerated by Graphical Processing Units. This reconstruction framework is an evolution of the architecture previously used in other studies [33], [34], [35].

We added TOF capabilities [5] to the reconstruction algorithm using the differences of timestamps in the events coincidences (Δt), binning in different histograms the coincidence and scatter events for each time bin used. During each MLEM iteration, we performed a forward and backward projection for each time bin, weighting the system matrix considering the time boundaries in each bin [36]. We used seven time-bins when TOF reconstruction was enabled.

As described above, this reconstruction method also allowed us to apply a scatter correction to the data. This is based on the double energy-window technique [37], [38] using the counts of the scatter events in the correction term of the MLEM algorithm. The scatter correction in the TOF version was implemented by simple scaling as described in [39], distributing in each time-bin the corresponding scatter counts using (1), where i indicates the LOR index, sc indicates the number of counts in the scatter histogram, and tr indicates the number of true coincidences counts for a given LOR i

$$\mathrm{sc}[i] = \mathrm{tr}[i] \times \left(\frac{\sum \mathrm{sc}[i]}{\sum \mathrm{tr}[i]} \right). \tag{1}$$

We reconstructed the images using a cubic voxel size of 2-mm size and 50 iterations, including the scatter correction, if not otherwise stated.

The workstation used during the reconstruction process was a high-performance computing server with two AMD EPYC 7282 CPU @ 2.80 GHz processors, 128 GB of RAM, 48 TB of available disk memory, and three NVIDIA GeForce RTX 3090 GPU CUDA capable devices. This computer had Windows 10 Pro (64 bits) as the operating system installed.

D. Performance Analysis

We carried out the performance analysis of the tested PET geometries following the NEMA NU 2-2018 protocol [40]. This protocol allows one to compare the performance of PET scanners under similar conditions, and in particular TOF-based systems. We provided comparative data with the PennPET and the Vision Quadra systems, introduced before, since they have similar FOV dimensions to the systems proposed here. Also, the uExplorer [41] has been included in the comparison. The PennPET system to which we compare our results is the one based on three rings of 16.4 cm each, separated by 7.4 cm. This system has some similarities to our 5 SR geometry. A second version of the PennPET scanner, with an extension of the axial length with the addition to a total number of 6 rings, have also been included in the comparison [18]. Table I

TABLE I
DIMENSIONS OF THE SCANNERS AND THEIR DETECTORS

Scanner	Crystal Dimensions (mm)	Scanner Dim (Diam x Axial)
IMAS 2 SR	25.4 × 3.1 × 20	82 cm × 21.1 cm
PennPET	3.86 × 3.86 × 19	76.4 cm × 64 cm
IMAS 5 SR	25.4 × 3.1 × 20	82 cm × 71.4 cm
IMAS 7 SR	25.4 × 3.1 × 20	82 cm × 74.7 cm
Vision Quadra	3.2 × 3.2 × 20	82 cm × 106 cm
PennPET v2	3.86 × 3.86 × 19	76.4 cm × 146 cm
uExplorer	2.76 × 2.76 × 18.1	78.6 cm × 194 cm

summarizes the crystal pixel sizes and geometries of these scanners.

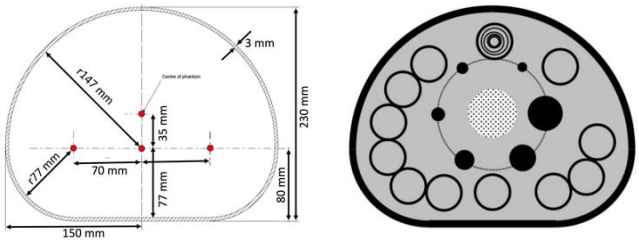

(a) (b)

Fig. 4. Sketch of the image quality phantom NEMA 2018. (a) Some dimensional details. (b) Distribution of VOIs in the volume.

E. Sensitivity

We simulated the 70-cm long linear ^{18}F source (diameter 0.25 mm). This linear source was encapsulated in a cooper cylinder with different thicknesses, so the total sensitivity value without the copper attenuation can be estimated by fitting all the sensitivities to an exponential absorption equation. Following the NEMA, we extracted for all the acquisitions an axial sinogram profile, calculating the distance of the LOR with the center of the axis. The activity of the source was 0.27 μCi to minimize random counts. Each acquisition lasted 16 min to collect enough coincidence events (around 107 kcounts). Then we calculated the sensitivity considering the total acquisition time and the number of registered coincidences. Additionally, we have calculated the sensitivity of a small 18F spherical source, with 0.25-mm diameter, placed at the center of the FOV with the same activity than the linear source.

F. Spatial Resolution

We estimated the spatial resolution with small (0.25-mm diameter) spherical ^{22}Na sources placed at different positions on the radial axis: 1 cm off-centered, 10 cm, and 100 cm. According to the NEMA, three acquisitions were performed at the axial FOV center and also shifted at 3/8 of the axial FOV. We did not perform filtered back projection (FBP) reconstruction, as NEMA suggests for these specific tests, since our previously developed FBP [27] algorithm cannot handle a large image size. Instead, we generated the images with the MLEM reconstruction algorithm, but using only ten iterations. This number of iterations represents a balance of achieving convergence of the spatial resolution with few iterations. This approach helps to prevent excessive iterations from converging the size of the reconstructed source to the voxel size. We evaluated the spatial resolution enabling and disabling the DOI correction to determine how much the parallax error was mitigated.

G. Noise Equivalent Count Rate and Time Resolution

The curve for the noise equivalent count rate (NECR) reflects the activity at which the scanner reaches the maximum count rate before accounting for saturation effects and, thus, a worsening of the image quality. We simulated a cylindrical high-dense polyethylene phantom at the center of the system FOV. Inside the phantom, a drilled cylindrical hole is filled with 18 kBq/mL of ^{18}F. While the radiation decays, a series of acquisitions were programmed, and a sinogram was generated for each measurement. Due to the well-known position of the radioactive source, it is possible to distinguish the contribution of the True events corresponding to the peak in the sinogram. The contribution of Random and Scatter events appears as a plateau below the peak. These data were also used to estimate the CTR of the system as a function of the activity in the system. This estimation was performed once we discarded the Random and Scatter from the CTR profile by extracting the bias below the Gaussian peak [40].

H. Phantom Studies

The torso phantom (also named image quality IQ) was simulated. It has a semi-cylindrical fillable geometry with different sections (see Fig. 4 left). Six fillable spheres of 10, 13, 17, 22, 28, and 37 mm diameter are placed at 114 mm from the phantom center. The background was filled with ^{18}F with a total activity concentration of 5.3 kBq/mL, whereas the activity concentration of the spheres was fourfold the background (4:1). The simulated total time of the acquisition was 400 s. We carried out the simulations on a Linux High-Performance Computing cluster composed of 161 computing nodes connected by a 10-Gb Ethernet network, summing up a total of 3220 CPU Intel Xeon cores and 18 TB of RAM memory.

To analyze the percentage contrast, we defined 12 spherical volumes of interest (VOIs) with 37 mm in diameter in the area beyond the hot spheres (2-mm slice). They are depicted in gray in Fig. 4 right. In each of them, several VOIs are placed concentrically with the diameters of the fillable spheres. Six additional VOIs are drawn for each hot sphere matching their size and depicted in the figure in solid black. We reconstructed the NEMA torso phantom using the MLEM algorithm, with and without TOF capabilities, enabling the scatter correction in both cases. We calculated the percent contrast (PC) as established by the NEMA using the following equation:

$$\text{Percent Contrast } (\%) = \frac{\left(\frac{\text{Mean Value VOI}}{\text{Mean Value Background}} - 1\right)}{\left(\frac{\text{Volumetric Activity VOI}}{\text{Volumetric Activity Background}} - 1\right)} \times 100. \quad (2)$$

Additional tests were performed using the so-called Jaszczack phantom to further evaluate the image quality. This

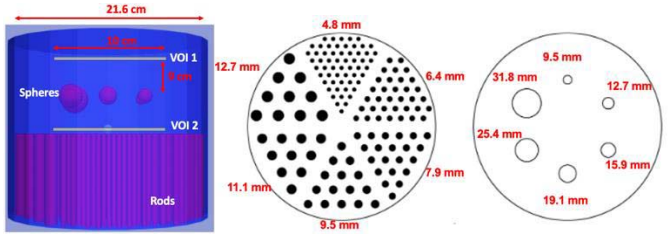

Fig. 5. Details of the Jaszczack phantom. (a) General dimensions of the phantom including the VOI for the uniformity study at + 9 cm and −9 cm with respect to the center of the hot spheres. (b) Sizes of the rods in the bottom part of the phantom. (c) Diameters of the hot spheres.

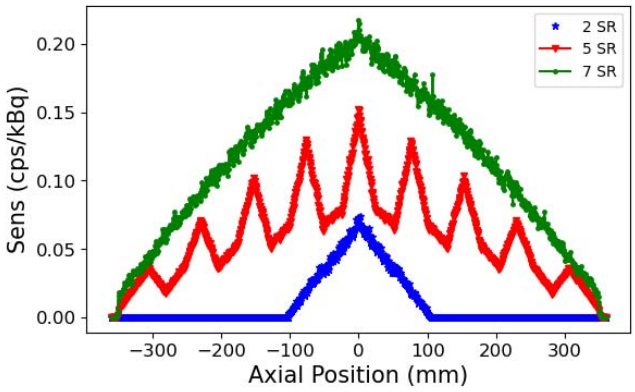

Fig. 6. Axial sensitivity profiles for 7, 5, and 2 SR obtained with a linear source.

phantom is divided into two parts, as shown in Fig. 5. The first part includes six groups of rods with different sizes: 4.8, 6.4, 7.9, 9.5, 11.1, and 12.7 mm (see Fig. 5 left). To estimate the accuracy in resolving the rods, we have calculated the Valley to Peak Ratio as shown in (3). We reconstructed this phantom using the MLEM algorithm, comparing the results also enabling and disabling the TOF capabilities

$$\text{Valley to Peak Ratio (\%)} = 100 * \frac{\text{Average Valley Voxel Values}}{\text{Average Peak Voxel Values}}. \tag{3}$$

The second section of the phantom is composed of a fillable cylinder of 216 mm in diameter and 186 mm height (see front view in Fig. 5 right). As for the torso phantom, the same cluster was employed to accelerate the simulation processes. The acquisition time of the simulation was 800 s. Inside this volume, six fillable spheres of different diameters are included, namely, 9.5, 12.7, 15.9, 19.1, 25.4, and 31.8 mm, respectively. The activity injected in the background volume was 370 MBq of ^{18}F. The volumetric activity ratio between spheres and background was set at 4:1. We generated a circular VOI for each sphere with the same diameter and location. We reconstructed this second section of the phantom with TOF and scatter correction; second, without TOF and with scatter correction; and without both TOF and the scatter correction. Then, we evaluated the PC defined in (2), for these sets of images. Using the Jaszczack phantom, we also evaluated the uniformity of the background area. Two cylindrical VOIs, with 10-cm diameter and 6-mm length, were defined in two different axial positions at +90 mm and −90 mm, see VOI1 and VOI2 in Fig. 5 left. The uniformity was estimated using the following expressions:

$$\text{Uniformity (\%)} = 100 \times (1 - \text{STD}) \tag{4}$$

$$\text{STD} = \frac{\text{STD}_{\text{ROI}}}{\text{Mean}_{\text{ROI}}}. \tag{5}$$

III. Results

A. Sensitivity

Fig. 6 depicts the sensitivity profile of the 70-cm linear source for all simulated configurations. For an energy window of 30% at the photopeak (350–650 keV), the 7 SR system registered 114 cps/kBq whereas the 5 SR version decreased to 58 cps/kBq and the 2 SR system reports 10 cps/kBq. As expected, the maximum value takes place at the center of the axial FOV and the sensitivity decreases at the edges of this. The results for the sensitivity obtained with a small spherical source at the system center are 6.8%, 14%, and 20% for the 2 SR, 5 SR, and 7 SR configurations, respectively.

B. Spatial Resolution

The spatial resolution remains below 3-mm full width half maximum (FWHM) for the whole FOV when DOI information is considered during the calibration and reconstruction processes. Without DOI, the radial and transaxial projections deteriorate to about 4.5 and 4 mm FWHM, respectively. Fig. 7 depicts the spatial resolution for the three space components for the 7 SR case, with and without DOI, both at the center of the axial CFOV and at 3/8. In Fig. 8, a comparison between the radial spatial resolution of the 7 SR, 5 SR, and 2 SR configurations is depicted, including DOI corrections.

C. Count Rates and Time Resolution

Fig. 9 shows the NECR results for the 7 SR and 5 SR configurations, including Trues and Random plus Scatter values. The NECR maximum values were found at 563 kcps and 563 kcps, for an activity concentration of 10 and 300 kBq/mL, for the 7 SR and 5 SR cases, respectively. The 2 SR system reports 100 kcps at 18 kBq/mL.

Fig. 10 shows the dependency of the CTR with the total activity, for the three configurations. We observe almost not deterioration once the Random and Scatter events are discarded. The median value of the CTR for the 7 SR scenario is 312.3 ps with a standard deviation of 1 ps. Both the 5 SR and 2 SR configurations exhibited a similar performance too.

D. Phantom Studies

The reconstruction of the NEMA IQ torso phantom is depicted in Fig. 11 for all the configurations making use of the TOF information and applying the scatter correction during the reconstruction process. PC values are plotted in Fig. 12 left for each sphere diameter for both with and without TOF capabilities for the 7 SR configuration.

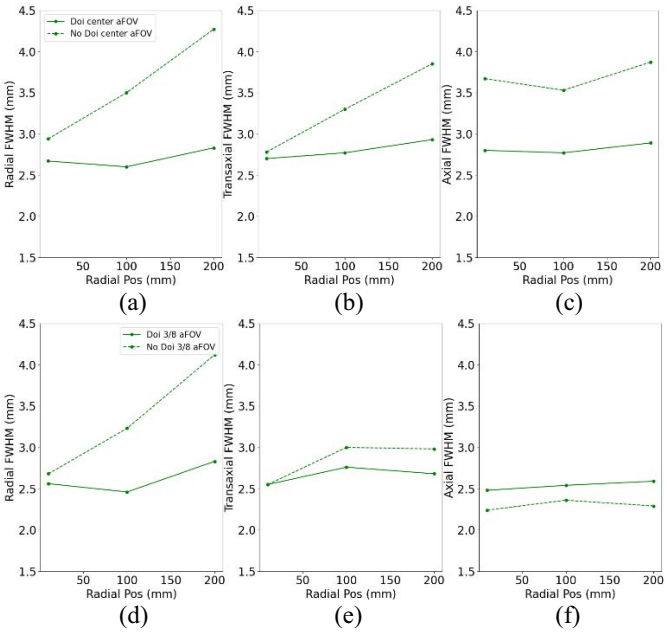

Fig. 7. Spatial resolution for the three axes with and without DOI correction (7 SR case). (a)–(c) At the center of the axial FOV. (d)–(f) At 3/8 of the axial FOV.

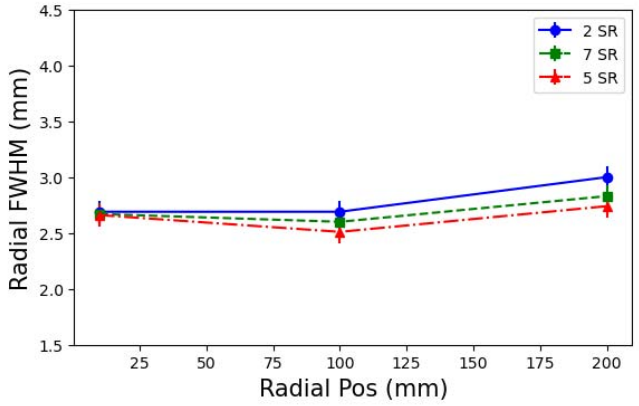

Fig. 8. Radial spatial resolution for the 7 SR, 5 SR, and 2 SR configurations, including DOI information.

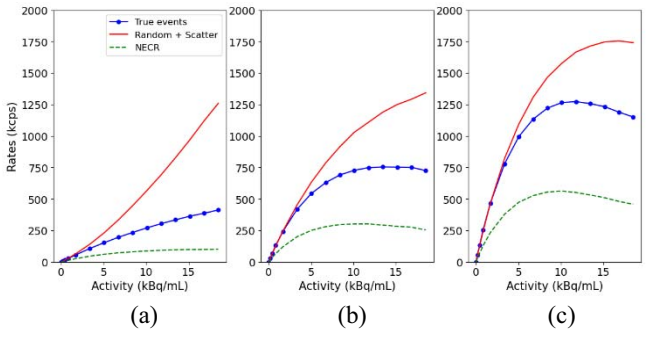

Fig. 9. Trues, Random + Scatter, and NECR curves for the IMAS 2 SR (a), 5 SR (b), and 7 SR (c) configurations. Notice the y-scale is in 10^6 units.

In Fig. 12 right, we compare the results for the PC for the simulated configurations. We observe a deterioration in the PC of the 5 SR scanner due to, most likely, a poorer uniformity of the images as a consequence of the gaps between rings.

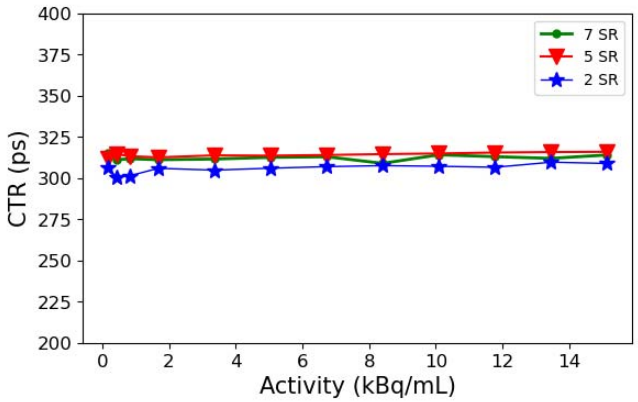

Fig. 10. CTR as a function of the activity for the three scanner configurations.

Fig. 11. NEMA image quality phantom reconstruction with TOF algorithm, for the (a) 2 SR, (b) 5 SR, and (c) 7 SR configurations.

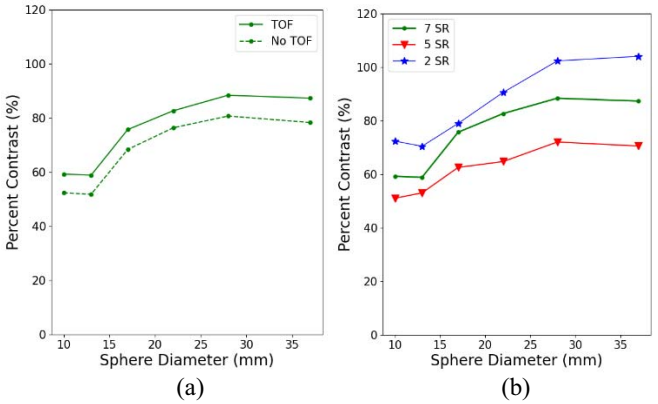

Fig. 12. (a) PC as a function of the sphere diameter for the 7 SR configuration. (b) Comparison of percentage contrast for the 7 SR, 5 SR, and 2 SR configurations.

One slice (1-mm thick) of the image reconstruction of the rods section of the Jaszczack phantom, including TOF, is shown in Fig. 13 for the three configurations. All the rods are clearly distinguished in the images. We have also included a comparison between the TOF reconstruction and non-TOF in Fig. 14 for the 7 SR configuration, together with a line profile across the smallest rods. Regarding the Valley to Peak ratio, we can observe that enabling TOF reconstruction the rods are better distinguished, characterized by an increased signal-to-noise ratio for the smallest inserts (see Fig. 15 left).

In Fig. 15 right, we have compared the Valley to Peak Ratio for all scanners. TOF and DOI correction were implemented

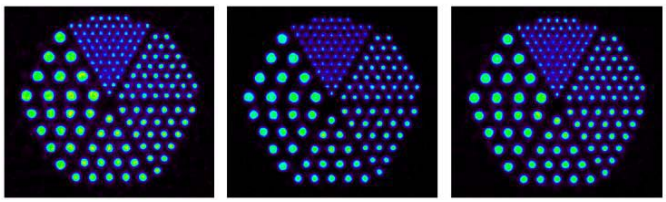

(a) (b) (c)

Fig. 13. Images of the rods section of the Jaszczack phantom with TOF. (a) 2 SR. (b) 5 SR. (c) 7 SR.

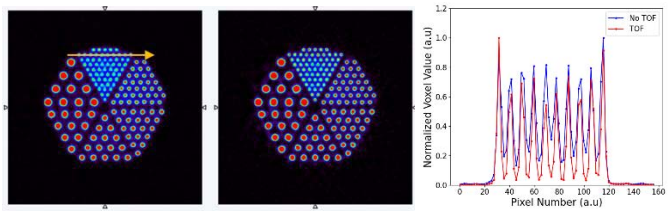

(a) (b) (c)

Fig. 14. (a) Slice (1 mm) of the reconstruction of the Derenzo-like section in the phantom without TOF for the 7 SR scanner. (b) Same slice but with TOF reconstruction. (c) Profile extracted along a row of rods of 4.8 mm in diameter.

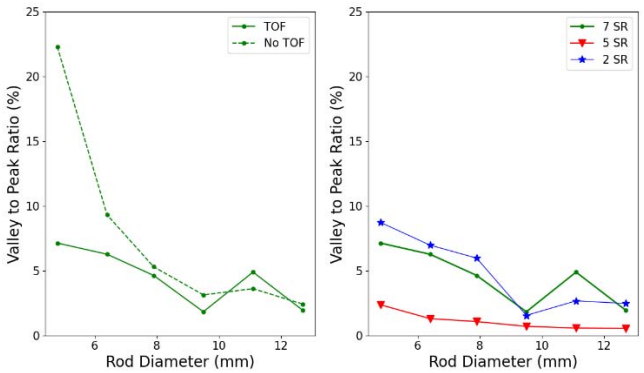

(a) (b)

Fig. 15. (a) VTP ratio as a function of the rod diameter for the 7 SR configurations, and for the TOF and non-TOF cases. (b) VTP with TOF reconstruction for all scanners configurations.

in the reconstruction process. To illustrate the impact of DOI on these phantoms, we present in Fig. 16 a side-by-side comparison of results with and without DOI, while keeping the TOF algorithm. A misposition of the rods is clearly observed, due to the parallax error.

In Fig. 17, we show again 1-mm thick slice of the image reconstruction corresponding to the other section of the Jaszczak phantom including TOF information, for the 7 SR configuration. When TOF and scatter correction are considered, we observe a PC larger than 80% for the smallest diameter and a 100% recovery for the largest sphere. In Fig. 17 bottom-right, the values of the PC for all simulated configurations are depicted.

Finally, the uniformity results are shown in Table II when the Jaszczack phantom is placed at the center of the FOV.

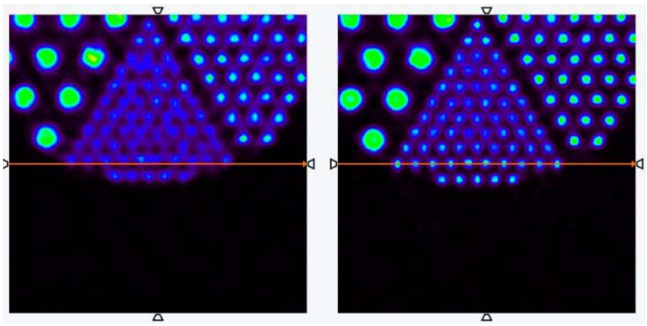

(a) (b)

Fig. 16. Reconstruction of the rods sections in the 7 SR scanner. (a) No DOI information. (b) Parallax error correction with DOI.

TABLE II
UNIFORMITY RESULTS FOR ALL THE SIMULATED SCANNERS

IMAS 7 SR	Upper ROI (%)	90.13
	Bottom ROI (%)	90.20
IMAS 5 SR	Upper ROI (%)	90.73
	Bottom ROI (%)	90.44
IMAS 2 SR	Upper ROI (%)	88.12
	Bottom ROI (%)	88.14

IV. DISCUSSION

Total Body PET scanners boost the system sensitivity by significantly increasing the axial coverage more than conventional scanners, whose axial length is typically in the range of 20–30 cm. All existing TB-PET scanners, except the J-PET system [42], make use of pixelated crystals, limiting the spatial resolution of their detectors to the pixel size and their ability to determine the annihilation photon DOI. However, they make it possible to achieve accurate CTR, and potentially apply TOF reconstruction algorithms. When implementing a detector blocks design based on semi-monolithic crystals, it is possible to introduce both DOI and TOF information simultaneously.

We initially tested this approach in simulations of a clinical scanner with 20-cm axial length, reaching interesting results in terms of spatial resolution and image quality. An extension of this work to a longer configuration reaching 70 cm has been proposed, with 7 and 5 rings. The second configuration includes gaps between rings. The initial sensitivity with 2 SR of 10 cps/kBq increases to 115 cps/kBq for the 7 SR configuration and to 58 cps/kBq for the 5 SR. As a comparison, the PennPET scanner with 7.4 cm gaps in the axial FOV [14] reaches 54 cps/kBq also due to the gaps between the rings in one of their configurations, whereas the Vision Quadra reports 175 cps/kBq due to its extended axial coverage of 106 cm.

The spatial resolution limit in clinical PET scans is influenced by the behavior of positrons. Previous studies affirm that, in clinical settings, the spatial resolution is affected by the acolinearity of the 2 gamma rays, resulting in a maximum achievable resolution of around 2 mm [13], [43]. It has also been demonstrated that, to reach this goal in long axial FOVs, it is necessary to perform an accurate DOI correction, since the parallax error increases due to the more obliquus LORs [13], [44]. Our findings are aligned with these statements since our results reach spatial resolution values of 2.6 and 3.0 mm when

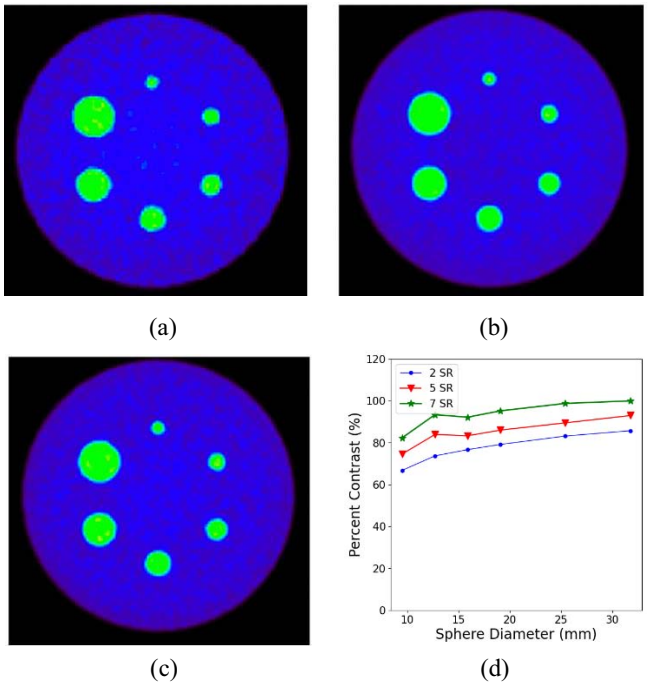

Fig. 17. One slice of the reconstruction of the Jaszczack phantom with TOF capabilities. (a) 2 SR. (b) 5 SR. (c) 7 SR. (d) PC for the three configurations as a function of the sphere diameter.

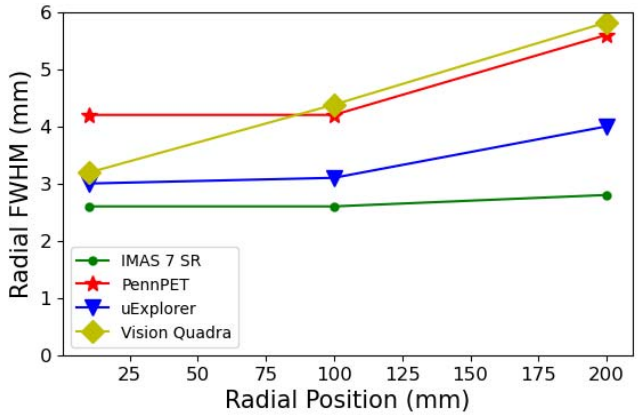

Fig. 18. Spatial resolution comparison for some total body PET scanners.

DOI correction is enabled (at 20 cm off radial center) for the 7 SR and 5 SR configurations, respectively. When DOI is considered and the parallax error is corrected, the spatial resolution for each axis trends to the same value, turning into a spherical shape.

The parallax error effect is well observed in the case of designs based on pixelated crystal arrays [43]. We can observe a deterioration when the source is far from the FOV (see Fig. 18). For instance, in the Vision Quadra, the radial spatial resolution worsens to almost 6 mm at 20 cm off-radial position. By using slabs, it is possible to mitigate the parallax error and keep a homogeneous spatial resolution response across the whole FOV.

As expected, by increasing the axial coverage from 20 to 70 cm, the NECR maximum value improves from 100 to 563 kcps for the 7 SR configuration and to 300 kcps for the 5 SR. This value is relatively low compared to the PennPET with gaps [17], which registers a maximum value of 1050 kcps at 38 kBq/mL, and the Vision Quadra with a NECR maximum of 2956 kcps at 28 kBq/mL. This could be a consequence of working with semi-monolithic crystals. In order to register the entire light distribution, a low energy threshold has been selected. In our case, all the events with more than 50 keV are accepted, increasing the deadtime and pileup events. For that reason, the NECR maximum is found at an activity of 10 kBq/mL. By increasing the energy threshold to 350 keV, both maximum NECR value and the optimum activity improve to 925 kcps at 17 kBq/mL, respectively. These values are similar to other scanners. The CTR estimation using the NECR phantom shows no degradation when the activity increases, once the random and scatter events were discarded, for all configurations tested.

TABLE III
COMPARISON OF NEMA 2018 RESULTS

Scanner	Sens (cps/kBq)	FWHM 10 (mm)	FWHM 200 (mm)	NECR (kcps @ kBq/mL)	Min. PC (%)	Max. PC (%)
IMAS 2 SR	10	2.7	2.9	100 @ 18.5	60	105
IMAS 7 SR	115	2.6	2.6	563 @ 10	60	89
IMAS 5 SR	58	2.7	3.0	300 @ 10	50	70
PennPET	54	3.9	5.6	1050 @ 38	30	75
Vis. Quadra	177	3.2	5.8	2956 @ 28	60	80
uExplorer	174	3.0	4.7	1524 @ 17	70	100
PennPET v2	140	3.9	5.6	2360 @ 44	35	75

We evaluated the image quality with two different phantoms. Using the NEMA 2018 image quality phantom (torso phantom), we have provided reconstructions with and without TOF capabilities, including attenuation and scatter corrections. Despite an artifact attributed to the simulation, the PC obtained in the analysis for the 7 SR configuration shows results comparable with the other scanners (see Table III). However, in the 5 SR configuration we observe that the PC is slightly deteriorated, most likely, due to the gaps between the rings. For this phantom, we have dealt with some difficulties during the simulation that we could not solve, and a slight artifact appears for all modeled configurations, as a line suggesting two background concentrations, as can be seen in Fig. 11. This issue becomes accentuated for the 7 SR scanner due to its higher sensitivity.

In the evaluation of the Jaszczak phantom, the rods sections were clearly resolved for all configurations. The PC for this phantom reached comparable values to the NEMA quality phantom. It is important to remark that the TOF algorithm enhances the results in both the Jaszczak and the NEMA torso phantoms.

As expected, the best PC for the Jaszczack phantom was obtained with the 7 SR, followed by the 5 and 2 SR configurations. However, the IQ phantom simulations showed that the 2 SR slightly improved the 7 and 5 SR configurations. These differences might be explained due to the number of intrinsic scatter events registered depending on the phantom size, where this process was more challenging for the larger axial FOV scanners in the case of the IQ phantom, which size is larger than the Jaszczack phantom

Table III summarizes the results of the simulation tests and compares them with real data obtained with the PennPET scanner (64 cm axial coverage), the Vision Quadra (106 cm axial), and the uExplorer (194 cm). The table includes the total registered sensitivity, the radial spatial resolution for the 10 and 200 mm off-centered positions, the maximum NECR and the activity where it takes place, as well as the minimum and maximum value of the PC obtained with the NEMA image quality phantom.

Despite the expected decrease in sensitivity of the 5 SR scanner, our simulation study has shown a comparable quality performance respect the 7 SR configuration, allowing to reduce the material costs without significantly affecting image quality. Our findings emphasize the importance of balancing scanner features and costs when designing a cost-effective long axial PET scanner. Therefore, it is crucial to consider the tradeoff between these factors carefully.

V. Conclusion

We have designed and tested with simulations a large axial FOV PET scanner with the ability to simultaneously estimate the DOI and reach an accurate CTR. We made use of semi-monolithic LYSO crystals instead of pixelated. By mitigating the parallax error, we observe an improvement in the spatial resolution performance for positions far from the radial center of the FOV. Furthermore, a CTR of 330 ps allows applying TOF algorithms to improve the image quality. We tested this new PET configurations following the NEMA NU 2 2018 protocol, which is more suitable for PET systems with TOF capabilities. The total sensitivity of the 7 SR configuration is about a factor of 10 larger than most conventional scanners due to the 70 cm axial coverage. The maximum NECR value is found at a rate of 563 kcps for the 7 SR and 300 kcps for the 5 SR, constrained by selecting low energy thresholds required to register the full scintillation light distribution. This value is higher than commercial scanners but lower than other long axial PET scanners. We are currently working on improving this feature by studying the advantages and disadvantages of increasing energy thresholds. Moreover, we have demonstrated that once the random and scatter events are discarded, the calculated CTR remains constant at 314 ps, for the range of tested activities. Including TOF capabilities in the reconstruction process results in a better image quality in both sections of the Jaszczack phantom, improving the VTP ratio and the PC. An improvement in the NEMA image quality phantom is also observed when the TOF is applied, reaching PC values better than other scanners.

In conclusion, the 7 SR and 5 SR scanner configurations show promising results using simulation tests following the NEMA protocol. Besides limited NECR values compared with other long axial FOV scanners, it registers an improved sensitivity than commercial systems. The combination of DOI information and the TOF algorithm leads to a high-quality image in both the Jaszczack phantom and the NEMA torso phantom.

Acknowledgment

All authors declare that they have no known conflicts of interest in terms of competing financial interests or personal relationships that could have an influence or are relevant to the work reported in this article.

References

[1] S. Basu, C. T. Kwee, S. Surti, A. Esma, D. Yoo, and A. Alavi, "Fundamentals of PET and PET/CT imaging," *PET/CT Appl. Non-neoplast. Cond.*, vol. 1228, no. 1, pp. 1–18, Jun. 2011, doi: 10.1111/j.1749-6632.2011.06077.x.

[2] M. A. Pysz, S. S. Gambhir, and J. K. Willmann, "Molecular imaging: Current status and emerging strategies," *Clin. Radiol.*, vol. 65, no. 7, pp. 500–516. 2010, doi: 10.1016/j.crad.2010.03.011.

[3] V. W. Pike, "PET radiotracers: crossing the blood-brain barrier and surviving metabolism," *Trends Pharmacol. Sci.*. vol. 30, no. 8, pp. 431–440, 2009, doi: 10.1016/j.tips.2009.05.005.

[4] X. Yu et al., "Requirements of scintillation crystals with the development of PET scanners," *Crystals*, vol. 12, no. 9, p. 1302, 2022, doi: 10.3390/ cryst12091302.

[5] S. Vandenberghe, E. Mikhaylova, E. D'Hoe, P. Mollet, and J. S. Karp, "Recent developments in time-of-flight PET," *EJNMMI Phys.*, vol. 3, no. 1, pp. 1–30, 2016, doi: 10.1186/s40658-016-0138-3.

[6] I. Rausch et al., "Performance evaluation of the Biograph mCT Flow PET/CT system according to the NEMA NU2-2012 standard," *EJNMMI Phys.*, vol. 2, no. 1, p. 26, 2015.

[7] L. R. MacDonald, W. C. Hunter, P. E. Kinahan, and R. S. Miyaoka, "Effects of detector thickness on geometric sensitivity and event positioning errors in the rectangular PET/X scanner," *IEEE Trans Nucl Sci*, vol. 60, no. 5, pp. 3242–3252, Oct. 2013, doi: 10.1109/TNS.2013.2278841.

[8] A. J. González, F. Sánchez, and J. M. Benlloch, "Organ-dedicated molecular imaging systems," *IEEE Trans. Radiat. Plasma Med. Sci.*, vol. 2, no. 5, pp. 388–403, Sep. 2018.

[9] Q. Xie, L. Wan, X. Cao, and P. Xiao, "Conceptual design and simulation study of an ROI-focused panel-PET scanner," *PLOS One*, vol. 8, no. 8, Aug. 2013, Art. no. e72109, doi: 10.1371/journal.pone.0072109.

[10] F.Muller, et al., "Walk-through flat-panel total body PET: System design and comparison of body motion with a standard PET-CT," in *Proc. 36th Annu. Congr. Eur. Assoc. Nucl. Med.*, 2023, pp. S259–S260.

[11] Z. Wang et al., "A high resolution and high sensitivity Prism-PET brain scanner with non-cylindrical decagon geometry," *J. Nucl. Med.*, vol. 62, no. 1, p. 1136, 2021.

[12] X. Zeng et al., "A conformal TOF-DOI Prism PET prototype scanner for high-resolution quantitative neuroimaging," *Med. Phys.*, vol. 50, no. 6, pp. 3401–3417, 2023.

[13] S. Vandenberghe, P. Moskal, and J. S. Karp, "State of the art in total body PET," *EJNMMI Phys.*, vol. 7, no. 1, pp. 1–33, 2020, doi: 10.1186/s40658-020-00290-2.

[14] S. Surti, A. R. Pantel, and J. S. Karp, "Total body PET: Why, how, what for?," *IEEE Trans. Radiat. Plasma Med. Sci.*, vol. 4, no. 3, pp. 283–292, May 2020, doi: 10.1109/TRPMS.2020.2985403.

[15] L. K. S. Sundar, M. Hacker, and T. Beyer, "Whole-body PET imaging: A catalyst for whole-person research?," *J. Nucl. Med.*, vol. 64, no. 2, pp. 197–199, 2023, doi: 10.2967/jnumed.122.264555.

[16] B. A. Spencer et al., "Performance evaluation of the uEXPLORER total-body PET/CT scanner based on NEMA NU 2-2018 with additional tests to characterize PET scanners with a long axial field of view," *J. Nucl. Med.*, vol. 62, no. 6, pp. 861–870, 2021, doi: 10.2967/jnumed.120.250597.

[17] J. S. Karp et al., "PennPET explorer: Design and preliminary performance of a whole-body imager," *J. Nucl. Med.*, vol. 61, no. 1, pp. 136–143, 2020, doi: 10.2967/jnumed.119.229997.

[18] B. Dai et al., "Performance evaluation of the PennPET explorer with expanded axial coverage," *Phys. Med. Biol*, vol. 68, no. 9, 2023, Art. no. 95007.

[19] G. A. Prenosil et al., "Performance characteristics of the biograph vision quadra PET/CT system with a long axial field of view using the NEMA NU 2-2018 standard," *J. Nucl. Med.*, vol. 63, no. 3, pp. 476–484, 2022, doi: 10.2967/jnumed.121.261972.

[20] I. Mohammadi, I. F. Castro, P. M. M. Correia, A. L. M. Silva, and J. F. C. A. Veloso, "Minimization of parallax error in positron emission tomography using depth of interaction capable detectors: Methods and apparatus," *Biomed. Phys. Eng. Exp.*, vol. 5, no. 5, 2019, Art. no. 62001, doi: 10.1088/2057-1976/ab4a1b.

[21] E. Yoshida et al., "Development of crosshair light sharing PET detector with TOF and DOI capabilities using fast LGSO scintillator," *Phys. Med. Biol.*, vol. 66, no. 22, 2021, Art. no. 225003.

[22] A. LaBella et al., "High resolution depth-encoding PET detector module with prismatoid light guide array," *J. Nucl. Med*. vol. 61, no. 10, pp. 1528–1533, 2020.

[23] T. K. Lewellen, "Recent developments in PET detector technology," *Phys. Med. Biol.*, vol. 53, no. 17, pp. 287–317, 2008, doi: 10.1088/0031-9155/53/17/R01.

[24] J. W. Cates and C. S. Lewis, "Evaluation of a clinical TOF-PET detector design that achieves < 100 ps coincidence time resolution," *Phys. Med. Biol.*, vol. 63, no. 11, 2018, Art. no. 115011.

[25] G. Cañizares et al., "Prior simulation test of a total body PET scanner with multiple configurations," in *Proc. IEEE Nucl. Sci. Symp. Med. Imag. Conf. (NSS/MIC)*, 2022, pp. 1–3.

[26] G. Santin et al., "GATE, a Geant4-based simulation platform for PET integrating movement and time management," in *Proc. IEEE Nucl. Sci. Symp. Med. Imag. Conf. NSS/MIC*, 2022, pp. 1516–1521.

[27] M. Freire et al., "Position estimation using neural networks in semi-monolithic PET detectors," *Phys. Med. Biol.*, vol. 67, no. 24, 2022, Art. no. 245011, doi: 10.1088/1361-6560/aca389.

[28] J. Barrio, N. Cucarella, M. Freire, C. Valladares, J. M. Benlloch, and A. J. Gonzalez, "Time and energy characterization of semi-monolithic detectors with different treatments and SiPMs suitable for clinical imaging," *IEEE Trans. Radiat. Plasma Med. Sci.*, vol. 7, no. 8, pp. 785–793, Nov. 2023, doi: 10.1109/TRPMS.2023.3300747.

[29] G. Cañizares et al., "Pilot results of detectors enhancing TOF and DOI capabilities, suitable for TB-PET," in *Proc. IEEE Nucl. Sci. Symp. Med. Imag. Conf. (NSS/MIC)*, 2021, pp. 1–3, doi: 10.1109/NSS/MIC44867.2021.9875550.

[30] F. H. Fahey, "Data acquisition in PET imaging," *J. Nucl. Med. Technol.*, vol. 30, no. 2, pp. 39–49, Jun. 2002.

[31] T. Yamaya et al., "DOI-PET image reconstruction with accurate system modeling that reduces redundancy of the imaging system," *IEEE Trans. Nucl. Sci.*, vol. 50, no. 5, pp. 1404–1409, Oct. 2003.

[32] L.A. Shepp and Y. Vardi, "Maximum likelihood reconstruction for emission tomography," *IEEE Trans. Med. Imag.*, vol. 1, no. 2, pp. 113–122, Oct. 1982.

[33] M. N. Cabrera-Martín et al., "Validation technique and improvements introduced in a new dedicated brain positron emission tomograph (CareMiBrain)," *Rev. Esp. Med. Nucl. Imagen. Mol. (Engl Ed)*, vol. 40, no. 4, pp. 239–248, 2021, doi: 10.1016/j.remnie.2021.05.001.

[34] L. Moliner, M. J. Rodríguez-Alvarez, J. V. Catret, A. González, V. Ilisie, and J. M. Benlloch, "NEMA performance evaluation of caremibrain dedicated brain PET and comparison with the whole-body and dedicated brain PET systems," *Sci. Rep.*, vol. 9, no. 1, 2019, Art. no. 15484, doi: 10.1038/s41598-019-51898-z.

[35] A.J. Gonzalez et al., "Initial results of the MINDView PET insert inside the 3T mMR," *IEEE Trans. Radiat. Plasma Med. Sci.*, vol. 3, no. 3, pp. 343–351, May 2019, doi: 10.1109/TRPMS.2018.2866899.

[36] A. Mehranian, F. Kotasidis, and H. Zaidi, "Accelerated time-of-flight (TOF) PET image reconstruction using TOF bin subsetization and TOF weighting matrix pre-computation," *Phys. Med. Biol.*, vol. 61, no. 3, pp. 1309–1331, 2016, doi: 10.1088/0031-9155/61/3/1309.

[37] M. S. Kuppuswamy and K. S. Nayak, "A scatter correction method for whole-body PET based on double-window filtering," *Phys. Med. Biol.*, vol. 51, no. 16, pp. 4039–4055, 2006.

[38] C. K. Hsieh and W. J. Chen, "A scatter correction method for PET using a double-window technique," *Phys. Med. Biol.*, vol. 54, no. 7, pp. 2097–2113, 2009.

[39] M. Conti et al., "First experimental results of time-of-flight reconstruction on an LSO PET scanner," *Phys. Med. Biol.*, vol. 50, no. 19, pp. 4507–4526, 2005, doi: 10.1088/0031-9155/50/19/006.

[40] *NEMA NU 2-2018 Performance Measurements of Positron Emission Tomographs*, Nat. Electr. Manuf. Assoc., Rosslyn, VA, USA, Jun. 2018.

[41] B. A. Spencer et al., "Performance evaluation of the uExplorer total-body PET/CT scanner based on NEMA NU 2–2018 with additional tests to characterize PET scanners with a long axial field of view," *J. Nucl. Med*, vol. 62, no. 6, pp. 861–870, 2021.

[42] S. Sharma et al., "Efficiency determination of J-PET: First plastic scintillators-based PET scanner," *EJNMMI Phys.*, vol. 10, p. 28, Apr. 2023.

[43] C. S. Levin and E. J. Hoffman, "Calculation of positron range and its effect on the fundamental limit of positron emission tomography system spatial resolution," *Phys. Med. Biol.*, vol. 44, no. 3, pp. 781–99, 1999.

[44] Z. Wang et al., "High-resolution and high-sensitivity PET for quantitative molecular imaging of the monoaminergic nuclei: A GATE simulation study," *Med. Phys.*, vol. 49, no. 7, pp. 4430–4444, 2022.